RSC Advances

PAPER

View Article Online
View Journal | View Issue

Cite this: *RSC Adv.*, 2022, **12**, 21690

Mitochondria-targeted alginate/triphenylphosphonium-grafted-chitosan for treatment of hepatocellular carcinoma

Kholoud K. Arafa,[a] Mohamed A. Hamzawy,[b] Shaker A. Mousa[c] and Ibrahim M. El-Sherbiny *[a]

Mitochondrial targeting of anticancer drugs can effectively eradicate chemotherapy-refractory cells through different mechanisms. This work presents the rational designing of mitochondria-targeted core–shell polymeric nanoparticles (NPs) for efficient delivery of doxorubicin (DOX) to the hepatic carcinoma mitochondria. DOX was electrostatically nano-complexed with sodium alginate (SAL) then coated with mitotropic triphenylphosphonium-grafted chitosan (TPP^+-g-CS) nanoshell. Polyvinyl alcohol (PVA) was co-solubilized into the TPP^+-g-CS solution to enhance the stability of the developed NPs. The optimum NPs formula is composed of TPP^+-g-CS (0.05% w/v) coating a DOX-SAL core complex (0.05% w/v), with 0.2% PVA relative to CS (w/w). The optimum NPs attained an entrapment efficiency of 63.33 ± 10.18%; exhibited a spherical shape with particle size of 70–110 nm and a positive surface charge which enhances mitochondrial uptake. FTIR and DSC studies results were indicative of an efficacious poly-complexation. *In vitro* biological experiments proved that the developed mitotropic NPs exhibited a significantly lower IC_{50}, effectively induced apoptotic cell death and cell cycle arrest. Moreover, the *in vivo* studies demonstrated an enhanced antitumor bioactivity for the mitotropic NPs along with a reduced biological toxicity profile. In conclusion, this study proposes a promising nanocarrier system for the efficient targeting of DOX to the mitochondria of hepatic tumors.

Received 23rd May 2022
Accepted 18th July 2022

DOI: 10.1039/d2ra03240f

rsc.li/rsc-advances

1. Introduction

Hepatic cancer has reached a daunting record for mortality rates counting for 8.3% of the total cancer deaths occurring in 2021 as reported by GLOBOCAN.[1] The mainstream for liver cancer treatment protocols relays at an early stage on surgery and drug chemotherapy. Despite the clinical advances achieved by such therapies, diverse drawbacks still hamper their curative efficacy. These include for instance the disease recurrence as well as the high metastasis rates encountered post-surgical resection of tumor masses. Additionally, in case of chemotherapy, the non-selective nature of drugs used can cause severe systemic toxicity leading to hazardous health effects. Therefore, the development of targeted antitumor drug platforms with maximal therapeutic activity concomitantly with minimal toxic side effects became imperative.

Recently, the application of nanomedicine in the treatment of various diseases is an expanding field of research. Advances in nanotechnology have profoundly benefited the biomedical as well as the pharmaceutical fields as it paved the road for modifying the drug's pharmacokinetic properties including solubility, bioavailability, diffusivity and release profile.[2] Consequently, the deployment of such nanostructured agents can lead to the betterment of their pharmacotherapeutic efficacy through improving the drug's biodistribution and cellular uptake, reducing the dose required and guarding against excessive drug metabolism.[3,4] The optimal design for the nano-scaled vehicle is principally based on the biophysical as well as biochemical properties of the loaded cargo.[5] Growing attention has be drawn towards the development of targeted drug delivery systems (TDDS) as it promote the accumulation of the loaded drugs at the desired site of action and ensuring their selective spatiotemporal release hence enhancing their therapeutic efficacy while reducing any undesirable effects.[6,7]

Most TDDSs have relied on the cellular biochemical distinctions between cancerous cells and their normal counterparts like the overexpression of specific surface receptors or antigens hence guarantying their specific recognition, interaction and uptake within the tumor mass.[8] Despite of the selective cellular deliverance, cellular-level targeting alone cannot ensure an enhanced therapeutic efficacy.[9] Thus, recently, subcellular

[a]*Nanomedicine Research Labs, Center for Materials Science (CMS), Zewail City of Science and Technology, Ahmed Zewail Road, October Gardens, 6th of October City, 12578, Giza, Egypt. E-mail: ielsherbiny@zewailcity.edu.eg*

[b]*Pharmacology & Toxicology Department, Faculty of Pharmacy, Fayoum University, Fayoum, Egypt*

[c]*Pharmaceutical Research Institute, Albany College of Pharmacy and Health Sciences, Rensselaer, NY 12144, USA*

TDDSs that are directed towards certain subcellular compartments have garnered scientific interest.[10] Among the various targetable intracellular organelles, we have chosen mitochondria as it significantly regulates the cellular homeostasis. Mitochondria control multiple physiological processes namely cellular respiration, metabolism, signaling, differentiation, apoptosis and intracellular Ca^{2+} levels.[11] To date several classes of mitotropic ligands were developed for targeting purposes including lipophilic cations namely dequalinium (DQA) and triphenylphosphonium (TPP^+).[12,13] Chemically, TPP^+ exhibits a unique structure composed of lipophilic phenyl groups as well as a phosphonium cation which endue it with specific mitochondrial accumulation.[14] The discovery of TPP^+ led to the formation of a plethora of mitotropic drug-conjugates as well as DDS.[15,16] Interestingly TPP^+ belongs to a class of salts known as quaternary phosphonium salts (QPS) which were reported to have antitumor effects against diverse cancer types including liver cancer.[17,18] Moreover, TPP^+ was found to preferentially amass in the tumor derived mitochondria due to their higher transmembrane potentials relative to their normal counterparts imparting it with advantageous therapeutic selectivity.[19]

Besides the targeting ligand, we have adopted doxorubicin (DOX) to be the model chemotherapeutic agent in this study. Intriguingly, DOX has been reported to act as a mito-active cytotoxic agent with the capability of mitochondrial accumulation aided by its specific binding to the phospholipid cardiolipin. Such DOX-mediated membrane perturbation inhibits complexes I and II deranging the electron transport chain (ETC) function. Additionally, the CI mediated reduction of the quinone moiety in the chemical structure of DOX into a reactive semiquinone free radical can derive the production of the deleterious reactive oxygen species (ROS) creating a vicious iteration of reactions known as the "redox cycling". Alternatively, DOX can further enhance ROS formation *via* interacting with iron to form reactive anthracycline–iron complexes through Fenton's reactions which ultimately disrupts normal iron homeostasis. Moreover, DOX can produce another class of reactive nitrogen species (RNS) *via* binding to endothelial nitrogen oxide synthase (eNOS) enhancing its activity which results in peroxynitrite ($ONOO^-$) free radical formation. Lastly, the mitochondrial DNA (mtDNA) repair enzyme, topoisomerase isoenzyme 1 is one of the main biotargets inhibited by DOX which leads to mitochondrial damage and cell death.[20]

Thus, in the present work, TPP^+ was selected as a mitochondria-targeting moiety and was conjugated to the hydrophilic chitosan (CS) polymer (TPP^+-g-CS). Then, mitochondria-targeted core–shell nanoparticles (NPs) were developed and optimized for efficient delivery of doxorubicin (DOX) to the liver mitochondria. Cationic DOX salt was electrostatically nanocomplexed with the negatively charged sodium alginate (SAL) followed by coating the obtained nanocore with the mitotropic TPP^+-g-CS nanoshell. Polyvinyl alcohol (PVA) was co-solubilized into the TPP^+-g-CS solution to improve the stability of the developed nanosystem. Besides, the obtained DOX-loaded core–shell NPs were optimized in such a way to have a net positive charge enhancing their delivery across the mitochondrial membrane. Next, the physicochemical, biological, morphological, and drug-encapsulating characteristics of drug-free and drug-loaded NPs were evaluated. Finally, the antitumor effect of TPP^+-decorated core–shell NPs against hepatocellular carcinoma was also investigated at both *in vitro* and *in vivo* levels.

2. Materials

Chitosan (MWT = 100 000–300,000, 89% deacetylated), sodium alginate (SAL), polyvinyl alcohol (PVA), (3-carboxypropyl)triphenylphosphonium bromide (TPP^+Br^-), *N*-hydroxysuccinimide (NHS), ethylcarbodiimide hydrochloride (EDC·HCl) and chloroform ($CHCl_3$) were obtained from Alfa Aesar. Doxorubicin hydrochloride (DOX.HCl), glacial acetic acid (CH_3COOH), hydrochloric acid (HCl), sodium hydroxide (NaOH) and triethylamine (TEA) were all bought from Sigma-Aldrich (St Louis, MO, USA).

3. Methods

3.1. Preparative procedure

3.1.1. Synthesis of TPP^+-g-CS polymer. The polymer preparation steps were inspired by the protocol developed by Huang *et al.* with few amendments.[21] Briefly, LMWT-CS (100 mg) was added to HCl-acidified water (100 ml, pH = 2.25) and left to stir until complete dissolution took place. Meanwhile, the TPP^+ was activated for 2 h using EDC/NHS aqueous solution. The activated TPP^+ solution was then centrifuged (10 000 rpm, 15 min) to remove excess EDC/NHS. Afterwards, pellet was resuspended in ultra-pure water and the TPP^+ solution was dropped onto the CS solution for which pH is adjusted to 4.7 using 1 N NaOH and left to stir over-night on ice (molar ratio 2 : 1 CS : TPP^+). Afterwards, the solution pH is raised to reach 9 using 1 N NaOH leading to precipitation of the grafted CS polymer which is in-turn collected *via* ultra-high-speed centrifugation (20 000 rpm, 20 min). The obtained pellet was washed twice with distilled water (2 cycles × 5 min) and centrifuged. Afterwards, the collected pellet was resuspended in water pH 4.7, frozen and freeze dried (brownish yellow powder).

3.1.2. Synthesis of the DOX-loaded NPs. The NPs were prepared following similar protocol to that reported previously with several modifications.[22,23] TPP^+-g-CS polymer was dissolved in 1% v/v acetic acid aqueous medium to obtain either 0.05 or 0.1% w/v solution. For polycomplexation, SAL polymer solution was prepared (0.1%, pH = 5.5). Also, DOX solution was prepared with the required concentration (1 mg mL^{-1}, pH = 8 using TEA). Firstly, DOX was introduced in a dropwise fashion to the SAL solution (ratio = 1 : 1 v/v) resulting in complex formation. Next, the formed complex solution was mixed into the TPP^+-g-CS polymer solution up on dropwise addition (ratio = 1 : 2 v/v) under homogenization to reach the desired final drug concentration. To increase the stability of the developed NPs, TPP^+-g-CS polymer was dissolved in PVA containing aqueous solution (0.2% w/w relative to CS) and the above scheme is repeated. Thus, four formulations **F1–F4** were obtained as displayed in Table 1.

Table 1 Composition of the developed NP systems

Code	TPP^+-g-CS (% w/v)	SAL : DOX (w/w)	SAL/DOX complex solution (% w/v)	PVA
F1	0.05	1 : 1	0.05	Absent
F2	0.05	1 : 1	0.05	Present
F3	0.1	1 : 1	0.1	Absent
F4	0.1	1 : 1	0.1	Present

3.2. Structural validation of TPP^+-g-CS

3.2.1. Proton nuclear magnetic resonance (^{1}H NMR). The sample was prepared by dissolving of TPP^+-g-CS conjugate (10 mg) in DMSO-d_6 ^{1}H NMR spectra were recorded at ambient RT on a JEOL EX300 300 MHz NMR spectrometer (Bruker Avance 300, Coventry, UK).

3.2.2. Fourier transform infrared (FTIR). The functional groups elucidation of TPP^+-g-CS conjugate was determined by FTIR spectroscopy scanning the frequency range of 600–4000 cm^{-1} (Frontier IR, PerkinElmer, USA).

3.2.3. Differential scanning calorimetry (DSC). The thermal behavior of NP's individual component was investigated using DSC including CS polymer, TPP^+ pristine powder and TPP^+-g-CS polymer (Pyris 6 DSC, PerkinElmer, USA). Samples were enclosed inside sealed standard aluminum pans and exposed to heat in a range of 40–400 °C at 10 °C min^{-1} increments. Samples were constantly purged with dry nitrogen at a rate 30 mL min^{-1}. An empty pan subjected to the same conditions was used as a reference.

3.3. Evaluation of the prepared core–shell NPs

3.3.1. Physicochemical characterization of NPs (FTIR and DSC). FTIR analysis was performed following the aforementioned operating protocol. The experiments were done on CS, plain drug and selected NPs. Moreover, DSC analysis was used to analyze plain DOX, blank NPs and DOX-loaded NPs.

3.3.2. Morphological examination of NPs. Transmission electron microscopy (TEM) was used for the morphological examination of selected NPs. A drop of the nanosuspension was placed onto a carbon coated copper grid, stained, and dehydrated using ethanol then visualized.

3.3.3. Particle size (PS), polydispersity index (PDI) and zeta potential (ZP) measurement. The PS, PDI as well as the ZP of the freshly prepared diluted core–shell NPs nanosuspension was evaluated by dynamic light scattering (DLS) spectroscopy using Malvern zetasizer. For each preparation, measurements were run in triplicates and mean values were recorded.

3.3.4. Drug entrapment efficiency (EE%). The amount of DOX entrapped inside the NPs was evaluated using the indirect assessment method. Where, the freshly prepared drug-loaded NPs were centrifuged (20 000 rpm, 30 min) at RT until complete pelleting of the NPs and separation from the rest of the solution (supernatant).

The concentration of DOX in the obtained supernatant was determined spectrophotometrically. All the measurements were repeated thrice. The drug EE% was mathematically estimated as follows:

$$\text{EE}\ (\%) = \frac{(\text{DOX})_{\text{total}} - (\text{DOX})_{\text{non-entrapped}}}{(\text{DOX})_{\text{total}}} \times 100 \quad (1)$$

where, $(DOX)_{total}$ denotes the theoretical weight of DOX initially added while $(DOX)_{non\text{-}entrapped}$ designates the amount of DOX remaining freely soluble in the supernatant.

3.3.5. *In vitro* drug release studies. Drug release experiments from DOX-SAL/TPP^+-g-CS NPs were run using a dialysis method. In brief, the cellulose membrane (MW cut-off = 12 000 Da; Severa) was hydrated overnight. Afterwards, the membrane was soaked in PBS for 1 h before the start of the experiment. Accurately weighed 10 mg of the dried NPs were reconstituted in PBS (2 mL) with adjusted pH. Next, the reconstituted sample was transferred into an Eppendorf tube, sealed tightly with the dialysis membrane and inverted upside-down into the receiving chamber. A 50 mL falcon tube (receptor compartment) was filled with 10 mL of PBS adjusted at specific pHs either to mimic the physiological environment (pH = 7.4) or the tumor microenvironment (TME, pH = 6.5). The entire system was continuously shaken (100 rpm, 37 °C). One mL aliquot was drawn from the receptor compartment at predetermined time points and the concentration of DOX released from the NPs was determined spectrophotometrically. The withdrawn sample volume was replenished with fresh release medium to keep the volume inside the receptor compartment constant during the entire experiment.

The cumulative percentage of DOX released at a particular time (t) can be calculated using the following equation:

$$\text{Cumulative DOX released}(\%) = \frac{(\text{DOX})_{\text{tp}}}{(\text{DOX})_{\text{total}}} \times 100 \quad (2)$$

where, $(DOX)_{tp}$ is the mass of the cumulative amount of released drug at specific time point and $(DOX)_{total}$ is the total mass of entrapped drug.

As controls, blank NPs were used, and the plain drug solution was deployed for comparison rationale applying the same above-mentioned procedure.

3.3.6. Drug release kinetics. The *in vitro* release data were fitted in different mathematical models to investigate the drug release kinetics utilizing the KinetDS software (version 3.0).[24]

3.4. *In vitro* biological analysis

3.4.1. Cell culture conditions. Human hepatic carcinoma cells (HepG2) were obtained from ATCC (American Type Culture Collection, VA, USA). Cells were grown in DMEM media supplemented with penicillin-streptomycin antibiotics (1%) and fetal bovine serum (FBS, 10%) under humidified CO_2 atmosphere (5% v/v, 37 °C).

3.4.2. *In vitro* cytotoxicity assay. Cytotoxicity assessment of the developed DOX-SAL/CS NPs (**F2′**) and DOX-SAL/TPP^+-g-CS NPs (**F2**) was done using MTT assay. First, HepG2 cells were seeded into 96-well plate (10^4 cells per well) and incubated overnight. Afterwards, aliquots of NP's suspension, in complete cell culture medium (100 μL), containing DOX at a desired

concentration range (0.01, 0.1, 1, 10, 100 μM) were applied to the cells and left to incubate for 48 h. Next, MTT solution (20 μL) was added to each well, mixed and incubated for 5 h. Finally, to assess viable cell count, absorbance peaks of the solubilized formazan dye was spectrophotometrically estimated (λ_{max} = 560 nm, corrected for background signals occurring at λ_{max} = 620 nm).

Additionally, HepG2 cells were incubated with SAL/TPP$^+$-g-CS NPs (as a negative control) using comparative NPs weight to their drug loaded counterparts and the rest of the experiment proceeded following similar procedures to the section above.

3.4.3. Tracking of NPs cellular uptake with fluorescence microscopy. To track the intracellular location of DOX-SAL/TPP$^+$-g-CS NPs (**F2**), Hep-G2 cells (0.25×10^6) were cultured on alcohol sterilized coverslips and incubated overnight to adhere. Afterwards, cells treatment with drug-loaded NPs (DOX concentration = 5 μM) was carried out for 12 h. Post treatment, the cell culture medium was washed away, and the cells were rinsed thrice using cold PBS (pH = 7.4). Afterwards, samples were dyed with MitoTracker Green FM (100 nM, 30 min, 37 °C) followed by DAPI nuclear staining (5 min). Cells were washed between different staining steps using cold PBS to eliminate excess dyes. Finally, viable cells were imaged using fluorescence microscopy (LABOMED fluorescence microscope LX400, cat no:9126000; USA). Image analysis was done using image-J software.

3.4.4. Measurement of cellular apoptosis. HepG2 cells (10^6) were treated with DOX-SAL/TPP$^+$-g-CS NPs (**F2**) for 48 h, a non-treated group was employed as a negative control. After treatment, cells were collected, rinsed with cold PBS (pH = 7.4) and resuspended in 400 μL calcium containing binding buffer. Next, Alexa-Fluor 488 annexin V/propidium iodide staining solution (Probes Invitrogen, Eugene, OR, USA) was applied to the cell suspension (15 min, dark conditions). Post-incubation, the cells (20 000 events per sample) were collected and analyzed in a FACScan flow cytometry analyzer. Excitation (λ = 488 nm) and the emission green fluorescence of AV (FL_1, λ = 530 nm, *x*-axis) and red fluorescence of PI (FL_2, λ = 575 nm, *y*-axis) were collected, respectively. Later, the obtained data were analyzed using the flow cytometry analysis software WinMDI 2.8.

3.4.5. Cell cycle analysis. DOX-SAL/TPP$^+$-g-CS NPs (**F2**) were applied on HepG2 cells (10^6) for 48 h, a non-treated group was employed as a negative control. Afterwards, cells were harvested, washed and fixed using cold ethanol (70% v/v) and kept on ice (30 min). Next, cells are collected, washed with cold PBS (pH = 7.4) and centrifuged (300–400 × g for 5 min). The obtained cell pellet is incubated in nucleic acid staining solution (500 μL, 30 min, RT). Next, one drop of ReadiDrop™ PI was added to the cells yielding a final dye concentration of 1 μg mL^{-1}. Finally, the cells were incubated for 10 min followed by analysis using flow cytometry.

3.5. *In vivo* biological studies

3.5.1. Animals. Adult Male, CD_1 mice (average weight = 25–30 g) were purchased from laboratory animal facility, Pharmacology and Chemistry Research Centre (PCRC), Misr University and Technology Park, 6th October City, Egypt. Before starting the experiment, the mice were acclimated for 10 days under 12 h light/dark cycles, controlled humidity, controlled temperature (22 ± 2 °C) and *ad libitum* feeding. The Institutional Animal Care and Use Committee, Fayoum University approved all *in vivo* experimental procedures with permit number (AEC 2102).

3.5.2. Induction of hepatocellular carcinoma (HCC). HCC was induced by intraperitoneal injection of *N*-nitrosodiethylamine (DEN, 200 mg kg^{-1}) in addition to subcutaneous injection of the tumor-inducing hepatotoxin carbon tetrachloride (CCl_4, 3 mL kg^{-1}) for six consecutive weeks. A total of 30 male CD_1 mice were randomly assigned to 6 groups. The first group (G_1) wild type and served as the negative control for the study. Otherwise, the remaining five groups (G_2–G_6) received intraperitoneal injection of DEN along with CCl_4.

3.5.3. Experimental design. Thirty male CD_1 mice were randomly assigned to 6 group (5 mice per group) as follows for ten weeks:

Group (1): served as non-treated control and received normal saline only (negative control).

Group (2): mice were treated with of DEN (200 mg kg^{-1}, i.p) and CCl_4 (3 ml kg^{-1}, s.c) for six consecutive weeks.

Group (3): animals were treated with SAL/TPP$^+$-g-CS NV carrier system, which is similar in composition to (**F2**) two times weekly for last consecutive 4 weeks. The aim of G_3 is to investigate the biological toxicity as well as the biological effect of the nanocarrier perse.

Group (4): mice were treated with DEN + CCl_4, then treated with free DOX·HCl (5 mg kg^{-1}, i.p) two times weekly for the last consecutive 4 weeks.

Group (5): mice were treated with DEN + CCl_4, then treated with DOX-loaded SAL/CS NPs (**F2′**) in a dose equivalent to (5 mg kg^{-1}, i.p) two times weekly for last consecutive 4 weeks.

Group (6): mice were treated with DEN + CCl_4 and DOX-loaded SAL/TPP$^+$-g-CS NPs (**F2**) in a dose equivalent to (2.5 mg kg^{-1}, i.p) two times weekly for last consecutive 4 weeks.

The results obtained from G_5 would confer a comparative stance to G_6 about the biological toxicity profile as well as the therapeutic efficiency of DOX-loaded mitochondrial NPs *versus* non-targeted counterparts.

3.5.4. *In vivo* serological tests. At the end of treatment period after 10 weeks, mice were anesthetized using ketamine (12.5 mg kg^{-1}) and xylazine (1.5 mg kg^{-1}). Afterwards, blood samples were collected from each mouse from retro-orbital vein under using non-heparinized microhematocrite capillary tubes and allowed to clot at RT. Next, samples underwent centrifugation (3000 xg, 20 min) to separate the serum and got stored at −20 °C until being used for serological assay. Treatment efficiency was monitored by measuring the tumor biomarker α-fetoprotein levels (AFP) using ELISA kit (Anogen, Mississauga, Ontario, Canada). Moreover, hepatic biomarkers levels namely alanine aminotransferase (ALT) and aspartate aminotransferase (AST) were evaluated using colorimetric kit (ProDia international, Germany). Whereas the serum level of the hepatic biomarker alkaline phosphatase (ALP) was estimated using kit (Biolabo SA, France).

3.5.5. *In vivo* histopathological examination. Animals will be euthanized under light anesthesia and their liver will be removed for histological examinations. Liver tissue specimens collected from various treatment groups were fixed in 10% neutral buffered formalin. Next, the fixed hepatic specimens were trimmed, washed, dehydrated in ascending grades of alcohol, cleared in xylene and embedded in paraffin. Afterwards, the specimens were sectioned (4–6 μm thickness) and stained by hematoxylin and eosin (H&E) for further microscopic investigation using light microscopy.

3.6. Statistical analysis

The statistical analysis was done using one-way Anova followed by Tukey's test (Sigma plot software 11.0). Statistical differences with ($P \leq 0.001$) denote extreme significance, ($P \leq 0.01$) denotes high significance and ($P \leq 0.05$) indicates statistical significance. Data were represented as mean ± SD.

4. Results and discussion

4.1. Preparation of TPP$^+$-g-CS conjugate

The TPP$^+$-g-CS conjugate was prepared as demonstrated in chemical synthesis Scheme 1. Initially, TPP$^+$ carboxylic group was activated through its reaction with the coupling reagents EDC.HCl followed by NHS thus forming an amine-reactive O-acyl-isourea intermediate then the more stable amine-reactive NHS ester, respectively. Subsequently, the produced NHS ester was added to an acidified aqueous solution of CS-polymer yielding the final desired conjugate (TPP$^+$-g-CS) connected *via* a stable amidic bond. The grafted polymer was collected through centrifugation followed by lyophilization (brownish yellow powder).

4.2. Structural validation of TPP$^+$-g-CS

^{1}H NMR spectrum of TPP$^+$-g-CS is shown in Fig. 1. Conjugation was affirmed due to the presence of signals between 7.80 and 8.57 ppm appearing at the aromatic region of the spectrum which are pertinent to the three phenyl rings of the newly introduced triphenylphosphonium groups.[25,26] However, the signals of the methylene protons in TPP$^+$ could not be distinguished clearly due to their relatively lower intensity and overlapping with the CS peaks at the aliphatic region of the spectrum.

FTIR spectra of TPP$^+$-g-CS, TPP$^+$, and CS from 500 to 4000 cm^{-1} are depicted in Fig. 2a. In TPP$^+$-g-CS, there was a new absorption peak presenting at 1548 cm^{-1} corresponding to the

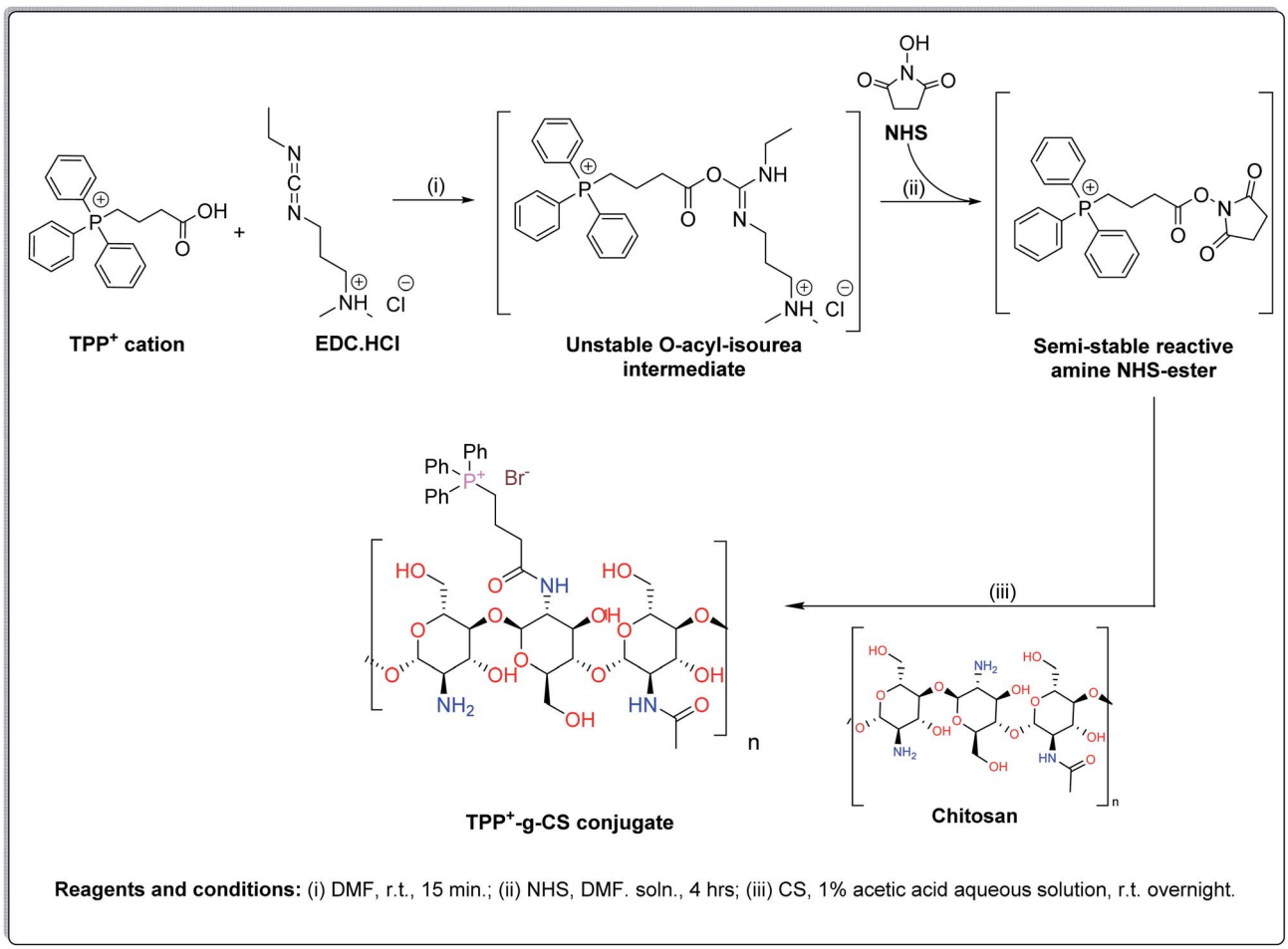

Scheme 1 Chemical synthesis steps of TPP$^+$-g-CS conjugate.

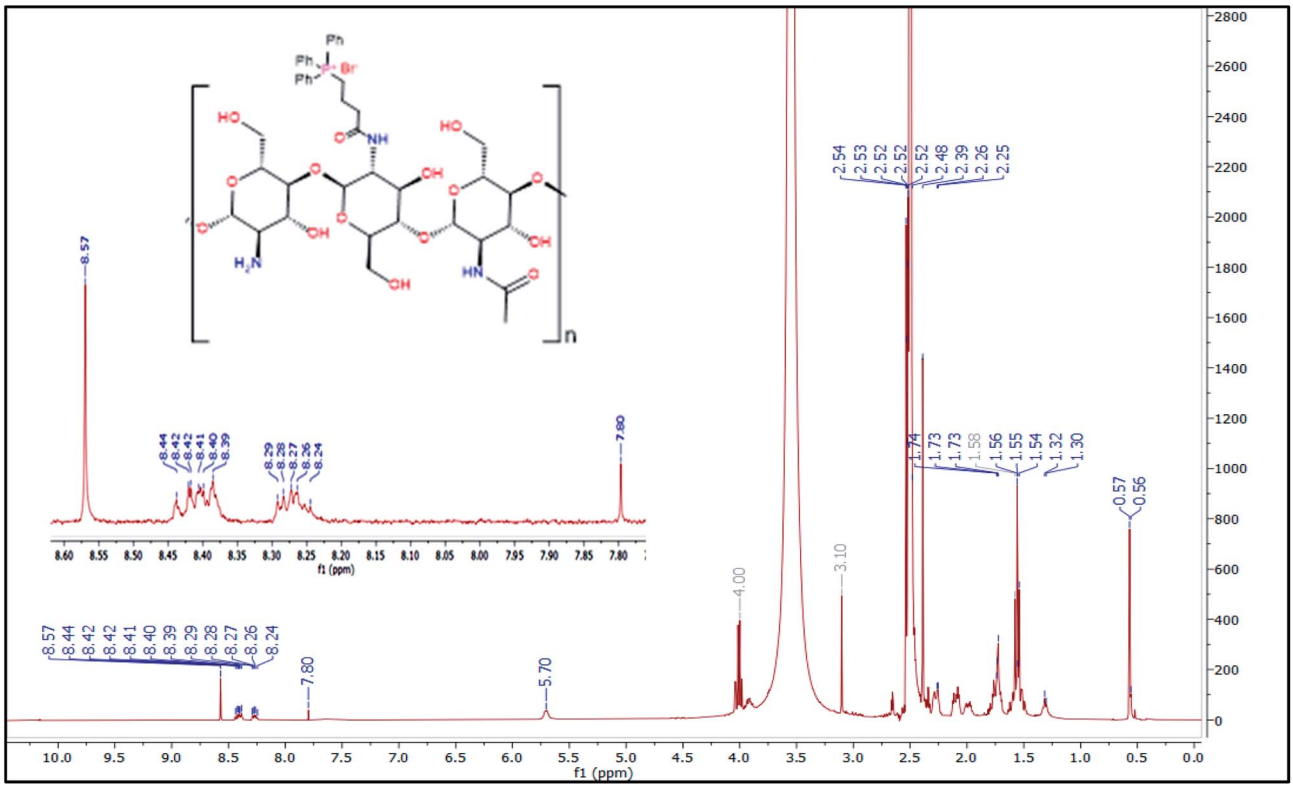

Fig. 1 NMR chart for TPP^+-g-CS polymer.

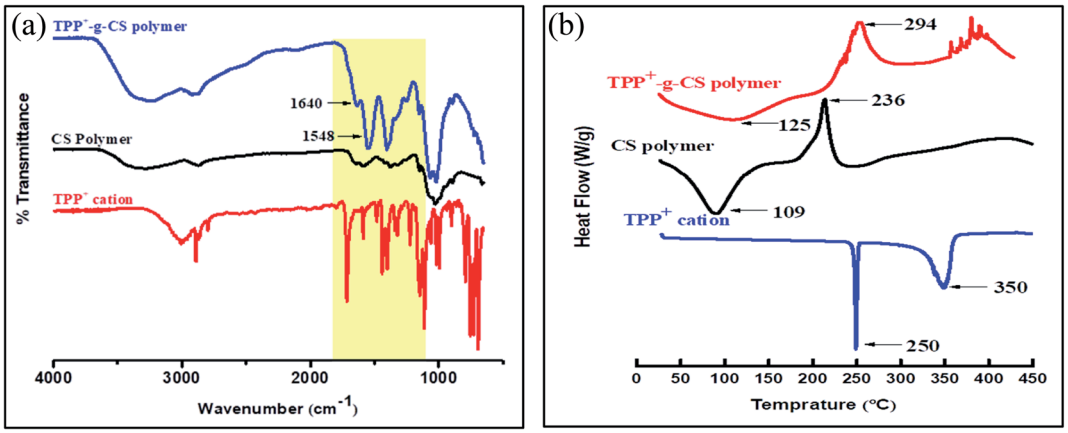

Fig. 2 (a) FTIR charts, (b) DSC thermograms for TPP^+, CS-polymer and TPP^+-g-CS conjugate.

absorption bands of the C=C of the phenyl rings pertinent to TPP^+ moiety.[25] Moreover, compared to the spectrum of CS, the appearance of additional peaks at 1640 cm^{-1} in the spectrum of TPP^+-g-CS, demonstrating that carboxylic group of TPP^+ mainly reacted with the amino groups of CS to form an amide bond.[27]

DSC thermograms are shown in Fig. 2b. First the CS chart demonstrated an endothermic peak at 109 °C indicating loss of hydration water as well as an exothermic signal at 236 °C indicative of the thermal decomposition of amine units in CS chains. As for the TPP^+ cation thermogram, two endothermic peaks at 250 °C (sharp) and 350 °C due to its melting and decomposition, respectively. Comparing the conjugate chart to its respective precursors, the bimodal endotherm at 124 °C with a fused shoulder 236 °C confirms the proper conjugation process. The observed decrease in intensity of endothermic peak at 125 °C, may indicate a reduction in the amount of water bound to the CS polymer post-conjugation due to consumption of free amino groups. Moreover, the broad endothermic peak at 352 °C can be attributed to the decomposition of TPP^+ moiety linked in the conjugate. Besides, the observed exothermic signal at 294 °C correlates to the residual unconjugated amine groups in CS backbone.

Table 2 Physicochemical characterization of developed drug loaded NPs

Code	PS (nm)	PDI	ZP (mV)	EE%
F1	542.9 ± 6.01	0.99 ± 0.06	34.00 ± 2.40	22.46 ± 5.32
F2	372 ± 4.72	0.39 ± 0.02	24.10 ± 0.71	63.33 ± 10.18
F3	521 ± 7.03	0.67 ± 0.04	31.05 ± 0.21	23.05 ± 2.69
F4	326 ± 2.91	0.44 ± 0.05	24.65 ± 0.78	50.43 ± 3.46

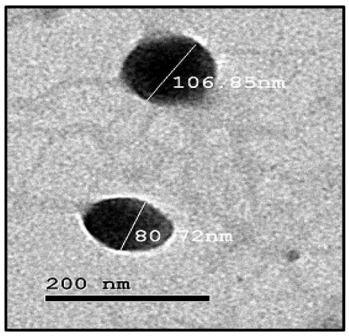

Fig. 3 TEM image of the DOX-SAL/TPP$^+$-g-CS NP (**F2**).

4.3. Particle size, surface charge and entrapment efficiency

Results of the particle size, surface charge and entrapment efficiency experiments are displayed in Table 2. It can be inferred from the obtained results that the presence of the PVA partially shielded the surface charge of the TPP$^+$-g-CS rendering it less positive, this observation is similar to previous literature.[28] PVA shielding of surface charge in turn affected particle size creating an observable pattern. Where, the highly positive NPs lacking PVA (**F1** and **F3**) tend to be unstable resulting in relatively high aggregate PS and widely distributed PDI. On the contrary, PVA addition to NPs (**F2** and **F4**) increased their stability and reduced their PS thus yielding a more homogenous population. Another pattern seen amongst PVA lacking NPs (**F1** and **F3**), is the direct proportionality of the PS to the CS percentage used; an effect that got moderated after PVA addition. Also, the drug entrapment followed a noticeable pattern, where the EE% increased with PVA addition (**F2** and **F4**) relative to the rest of the developed NPs (**F1** and **F3**). The observed results might be attributed to increased NPs stability. From the obtained results of physicochemical characterization **F2** formula was considered optimum and hence was selected for further studies.

4.4. Morphological investigation (TEM images)

TEM images of the DOX-SAL/TPP$^+$-g-CS NP (**F2**) demonstrated that the particles exhibited a spherical morphology with the size range (80–110 nm). The observed NPs size was lower than that measured using DLS. DLS obtained results might reflect the hydrated particle size (372 nm with PDI values 0.391), Fig. 3. As reported repeatedly, TEM imaging is considered the technique of choice to accurately assess NP's PS as it depends on direct high-resolution visualization of particles. Moreover, artifacts affecting the quality of DLS measurements including solution dynamics, NPs aggregation, presence of hydration shells by the surrounding solvent as well as Brownian motion induced fluctuation in light-scattering are well eliminated.[29] Therefore, PS obtained by TEM imaging were selected over DLS.

4.5. Physicochemical characterization of NPs

The absorption spectrum for pristine DOX shows a characteristic band at 1722 cm^{-1} (C=O bond stretching) at atom C-13. The peaks occurring at both 1575 and 1615 cm^{-1} (C=O bond stretching and bond vibration) of the anthracene ring, respectively. Moreover, the wide band observed at 3360 cm^{-1} signals overlapped peaks (–OH and –NH$_2$ groups vibration). As for DOX-SAL/CS NPs chart, the peak at 3298 cm^{-1} is similarly present in the parent TPP$^+$-g-CS and the nanovoid (NV) confirming proper formation of NPs. Moreover, the disappearance of 3360 cm^{-1} related to the pristine DOX confirms the effective physical entrapment of the drug inside the NPs, Fig. 4a. Additionally, the occurrence of peaks at 1588 and 1405 cm^{-1} were observed. Conclusively, FT-IR charts indicate the electrostatic interactions between DOX, SAL and CS.

DSC was employed to understand the thermal behavior of the developed DOX-SAL/CS NPs and to elucidate possible interactions between the different constituting polymers along

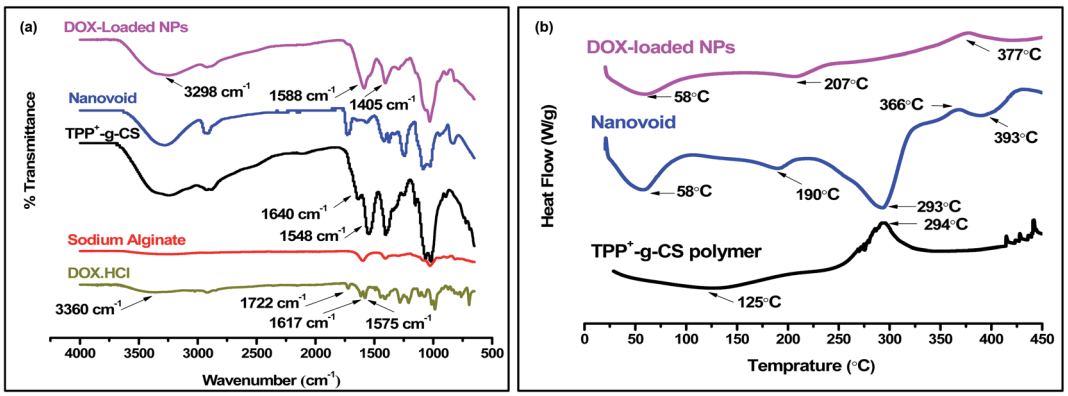

Fig. 4 (a) FTIR charts, (b) DSC thermograms of SAL/TPP$^+$-g-CS NPs (DOX-loaded and NVs) along with precursor pristine polymers.

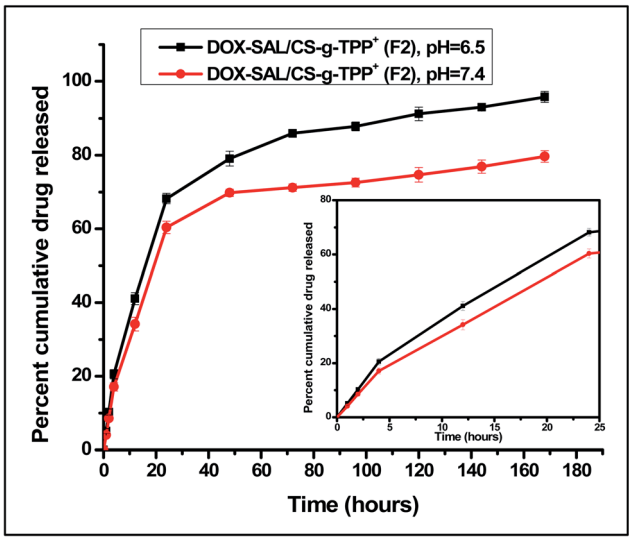

Fig. 5 Cumulative release profiles of drug from the developed DOX-SAL/TPP$^+$-g-CS core shell NPs in two different pHs (6.5 and 7.4).Inset is the release profile during the first day. Results presented as Mean ± SD (n = 3).

with the drug. Generally, the endothermic peaks around 100 °C are mainly associated with the dehydration of the hydrophilic molecules. The obtained thermograms demonstrate a minor lowering in the melting endotherm observed in the developed NPs relative to pristine TPP$^+$-g-CS polymer which confirms the formation of NPs. Furthermore, comparing the thermogram of NVs to that of DOX-loaded CS NPs reflects the disappearance of the endothermic peak at 293 °°C as well as the step change at 377 °C suggesting that the electrostatic interactions occur between DOX, the carboxylic groups of SAL and the amino-groups of CS. Moreover, DOX-loaded NPs thermogram was showing a minor endothermic peak at 207 °C that might be DOX-related endothermic melting peaks indicating the proper inclusion of drug in the polymer, Fig. 4b.

4.6. *In vitro* drug release experiments

The prepared DOX-loaded core–shell NPs (**F2**) revealed a sustained release profile of the drug that lasted for 168 h, Fig. 5. Moreover, the results demonstrated that the cumulative drug release rate was significantly greater at the TME mimicking acidic environment (pH = 6.5) in comparison to physiological conditions (pH = 7.4), $P < 0.05$. The obtained findings suggest that there is a relative spatial selectivity in drug release within the cancerous niche.

To completely comprehend the kinetics of drug release, the empirical results were fitted using mathematical modeling, Table 3. Modeling outcomes showed that all the tested NPs predominantly followed the Korsmeyer-Peppas model pertinent to polymeric systems (R^2 = 0.999). Where, the numerical value of the diffusional exponent (n) can predict the drug-release mechanism. Conventionally, Fickian diffusion is represented by ($n \leq 0.5$) whereas, non-Fickian model can be either anomalous transport ($0.5 < n < 1$), case-II transport ($n = 1$) or super case-II transport ($n > 1$).[30] Conclusively, the obtained release exponent $n > 1$ reflects a non-Fickian drug release follows super case-II transport that is controlled through polymer swelling and relaxation.

Table 4 Cytotoxic effect on HepG2 hepatocellular carcinoma cells

Formula	IC_{50}
SAL/TPP$^+$-g-CS NV	N.D.
DOX-SAL/CS NP (**F2′**)	12.94 ± 0.68
DOX-SAL/TPP$^+$-g-CS NP (**F2**)	3.86 ± 0.20
Plain DOX	2.22 ± 0.12

4.7. Biological assessments

4.7.1. Cytotoxicity results. To determine the cytotoxic concentration of the TPP$^+$-g-CS based NPs, HepG2 hepatocellular carcinoma cells were treated by the NPs either drug free (as negative control) or drug loaded NPs under the same conditions also non-grafted-CS NPs (**F2′**) and free DOX were tested (as positive controls), Table 4 and Fig. 6. The concentration depicted on the horizontal axis is equivalent to DOX in the NPs and a similar weight of NV was taken as a negative control. From the obtained results it was found that DOX-SAL/TPP$^+$-g-CS NPs (**F2**) were the most efficient to significantly reduce cell viability (IC_{50} = 3.86 ± 0.20 μM) as compared to the non-grafted-CS NPs (**F2′**) exhibiting 3-fold lower cytotoxicity (IC_{50} = 12.94 ± 0.68 μM, P = 0.001). The obtained findings prove the higher efficiency of mitochondrial targeting in inducing cancer cells death. Furthermore, to test the biocompatibility of the

Table 3 Kinetic fitting model results

		DOX-SAL/TPP$^+$-g-CS (**F2**)	
Mathematical model	Equations	pH = 6.5	pH = 7.4
Zero order	$Q = k{\cdot}t + Q_0$	0.734	0.717
1st order	$Q = Q_0\, e^{k\cdot t}$	0.146	0.146
2nd order	$(1/Q) = k{\cdot}t + 1/Q_0$	0.088	0.088
3rd order	$(1/Q)^2 = k{\cdot}t + 1/Q0^2$	0.088	0.088
Korsmeyer–Peppas	$\boldsymbol{Q = k{\cdot}t^n}$	**0.999**	**0.999**
Hixson–Crowell	$(1/Q)^{1/3} = k{\cdot}t + 1/Q0^{1/3}$	0.522	0.514
Baker–Lonsdale	$3/2 \times [1 - (1 - Q)^{2/3}] - Q = k \times t$	0.796	0.708

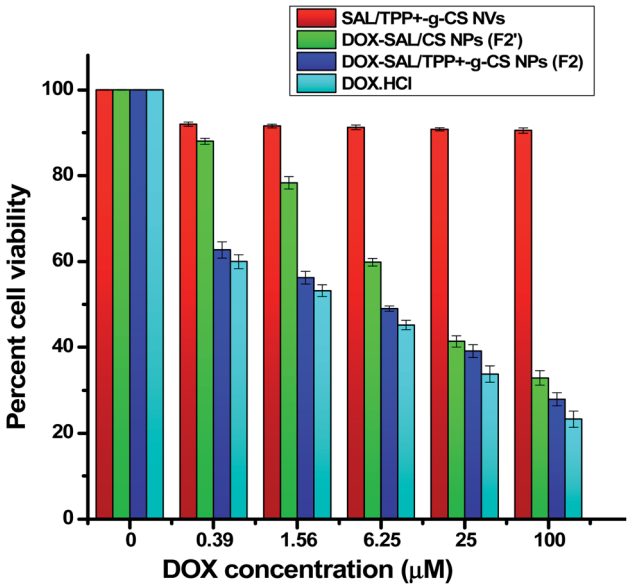

Fig. 6 Cytotoxicity of the developed DOX-loaded NPs (IC_{50}) relative to nanovoid and DOX using HepG2 hepatocellular carcinoma cells. Results presented as mean ± SD ($n = 3$).

developed TPP^+-g-CS NPs, the NVs were applied to the cells and were proven non-toxic to cells perse.

4.7.2. Fluorescence imaging and cellular uptake results. To track, visualize and quantify the intracellular localization of DOX-SAL/TPP^+-g-CS NPs (**F2**), HepG2 intracellular organelles were dyed with nuclear labelling stain (DAPI, dark blue color) and mitotracker (green color) fluorescent dyes, Fig. 7. As shown in microscopic images, **F2** NPs were successfully internalized by the treated cells as presented for fluorescence pertinent to DOX (red color). Intriguingly, the drug was found to almost exclusively localized in the mitochondria which is evident in the merged field resulting in yellow pseudo-fluorescence. Based on image analysis and areas overlay measurements, red-green areas overlay percentage was found to be 85.299% confirming the extensive mitochondrial uptake of the targeted **F2** NPs. On the contrary, red-blue areas overlay was merely 1.074% indicating the poor nuclear localization of the DOX-loaded NPs.

4.7.3. Apoptotic cell death analysis results. Cells undergoing apoptosis can be detected through investigating the inversion of the membrane phospholipid, phosphatidylserine (PS), from the internal membrane side to the external membrane surface. This phenomenon is assessed *via* co-staining the cells with annexin-FITC which binds to the externalized PS and propidium iodide (PI) which exclusively intercalates the DNA of permeable dead cells. Accordingly, HepG2 liver carcinoma cells were subjected to DOX-SAL/TPP^+-g-CS NPs (**F2**) using the reported IC_{50} for 48 h. While non-treated cells were deployed as negative control. Results, presented in Table 5 and Fig. 8, show that the treatment elicited apoptotic programmed cell death with significant 26.08% decline in cell viability ($P = 0.001$). Early apoptotic sub-population percentage was 3.62%, which is 7.86-fold higher than the non-treated control ($P = 0.001$). Furthermore, dual stained late apoptotic cells percentage was 14.25% ($P = 0.001$), which is approximately 55-fold higher than the negative control. Collectively, it can be concluded that the applied optimal NPs effectively elicited programmed cell death in HepG2 cells. Besides, a significant increase in necrotic sub-population was observed counting for 9.54% which is almost 16-fold higher than their non-treated counterparts ($P = 0.001$).

4.7.4. Cell cycle analysis results. The treatment elicited changes in the cellular distribution among different cell-cycle

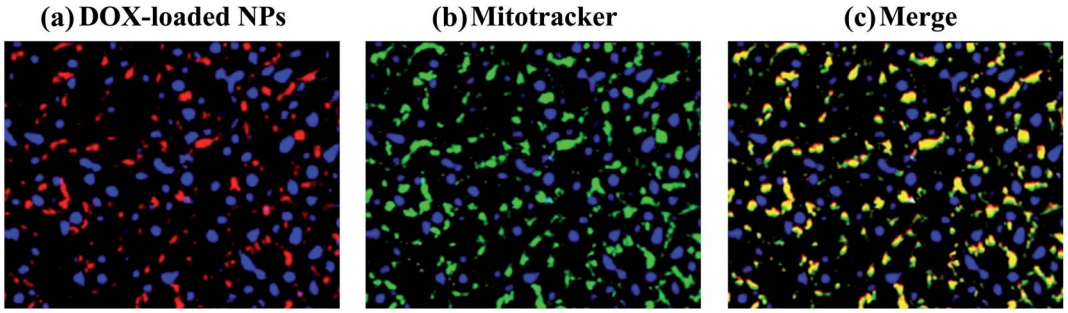

Fig. 7 Intracellular distribution of DOX-SAL/TPP^+-g-CS NPs monitoring by fluorescence microscopy. HepG2 cells incubated with DOX-loaded TPP^+-g-CS NPs (**F2**) for 12 h. (a) **F2** NPs (DOX: 5 μM, red); (b) mitochondrial staining by mitotracker (100 nM, green); (c) merged images (a and b). Nuclear labelling by DAPI (dark blue) present in all fields. Scale bar 100 μM.

Table 5 Apoptosis flow cytometric profiling upon treatment of HepG2 cancer cells with (F2)

		Apoptosis		
Sample	Normal	Early	Late	Necrosis
Non-treated Control	98.67 ± 1.04	0.46 ± 0.08	0.26 ± 0.04	0.61 ± 0.05
DOX-SAL/TPP^+-g-CS NPs (**F2**)	72.59 ± 1.36	3.62 ± 0.51	14.25 ± 0.79	9.54 ± 0.39

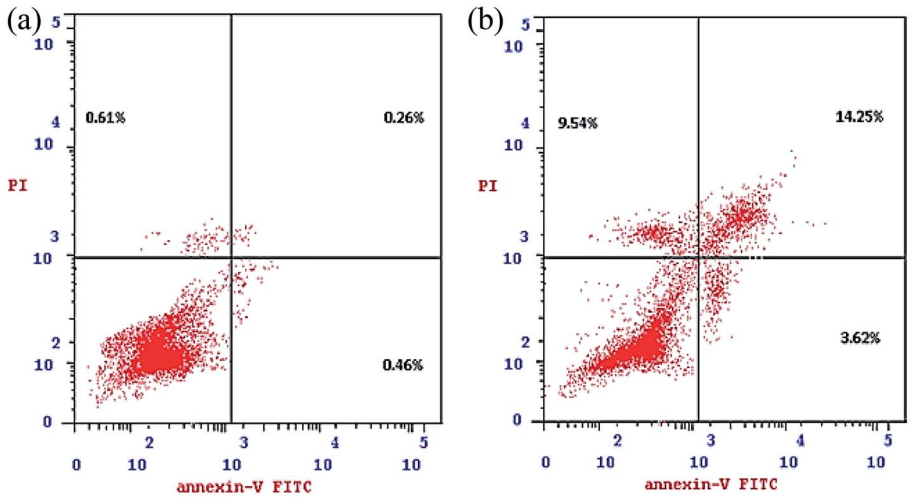

Fig. 8 Apoptosis induction cytograms for (a) non-treated control HepG2 cells; (b) DOX-SAL/TPP$^+$-g-CS NPs (**F2**) treated HepG2 cells (3.86 ± 0.20 μM, 48 h). Results are presented as mean ± SD ($n = 3$).

Table 6 Cell population distribution over the various cell cycle phases upon treatment of HepG2 cancer cells with (**F2**)

Sample	%G_0–G_1	%S	%G_2/M	%Pre-G_1
Non-treated Control	46.27 ± 1.85	34.02 ± 2.33	19.71 ± 1.88	1.33 ± 0.41
DOX-SAL/TPP$^+$-g-CS NPs (**F2**)	42.27 ± 1.91	56.31 ± 1.60	1.42 ± 0.29	27.41 ± 1.72

phases was investigated *via* implementing the DNA content flow cytometric analysis. Results showed that HepG2 cells treated by DOX-SAL/TPP$^+$-g-CS NPs (**F2**) accumulated at the pre-G1 phase recording an almost 20-fold increase comparative to non-treated control cells. The findings suggest that the genetic material underwent degradation proving that the NPs have an effective apoptosis mediated anti-proliferative activity ($P = 0.001$). The results observed conform well with our conclusions inferred from apoptosis analysis. Furthermore, cell-cycle arrest at S-phase was also noticed with 1.65-fold increase in cell population relative to control ($P = 0.001$) concomitant with a significant reduction in G2/M-phase population, obtained are similar to previous reports.[21] The obtained result suggests intervention with DNA replication associated with decreased cell-population in the G2/M-phase. Meaning, our DOX-loaded NPs target ($4n$) S-phase cells at chromosomal replication stage leading to enhanced DNA binding capability leading to inability to ensue to the subsequent phase. Results are displayed in Table 6 and Fig. 9.

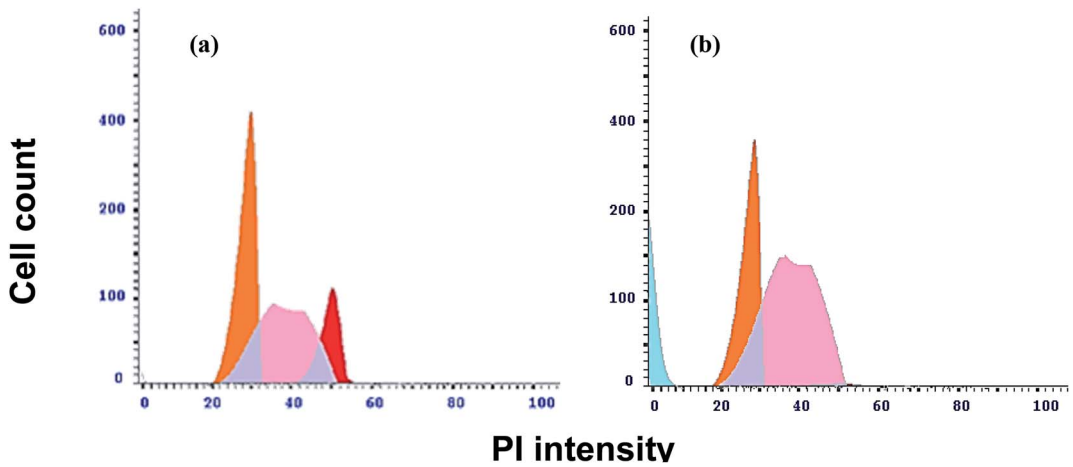

Fig. 9 Cell cycle analysis cytograms of (a) non-treated control HepG2 cells; (b) DOX-SAL/TPP$^+$-g-CS NPs (**F2**) treated HepG2 cells (3.86 ± 0.20 μM, 48 h). Results are presented as mean ± SD ($n = 3$).

4.7.5. *In vivo* HCC-induction and biochemical analysis results. Hepatic tumors were induced in the mice using *N*-nitrosodiethylamine (DEN). α-Feto protein (AFP) measurements in blood were implemented weekly to confirm successful tumor induction, Fig. 10a. The expression of AFP is directly correlated with hepatocyte differentiation and is considered as the standard noninvasive diagnostic biomarker for HCC progression.[31] Tumor formation took 10 weeks and was further confirmed through histopathological examination of the liver tissues, Fig. 11b. Physiologically, DEN is metabolically bioactivated in the liver to produce O^6-ethyl deoxyguanosine as well as O^4- and O^6-ethyl deoxythymidine. The formed metabolites form irreversible DNA adducts leading to carcinogenesis.[32] Additionally, to ensure proper initiation of HCC the hepatotoxin carbon tetrachloride (CCl_4) was introduced. Mechanistically, CCl_4 increases the endotoxin levels which promote the development of hepatic inflammation and fibrosis that are reportedly mediated by the ROS activation and biochemical signaling aberrations.[33] As a tumor promoter, CCl_4 reduces the time required for tumor formation.[34] The obtained findings demonstrated severe liver damage of AFP significant protein level increase post-injection with hepatotoxins DEN + CCl_4 relative to normal group ($P < 0.0001$). A significant incremental decrease in AFP level was observed upon treatment with free DOX.HCl, as compared to the normal control ($P < 0.05$). Remarkably, G_5 and G_6 treated with non-grafted-CS NPs (**F2′**) and TPP^+-g-CS NPs (**F2**) reverted to normal physiological AFP serum levels. Since several studies confirmed a direct proportional relation between serum AFP and severity of liver disease clinically, it can be concluded that **F2** possesses the most therapeutic efficiency.[35]

Post tumor induction, a dose titration study was implemented to figure out the effective lethal dose (EC_{50}) of the free DOX.HCl (G_4) as well as the DOX-loaded core–shell NPs (G_5, G_6). The obtained findings showed that both the free drug (G_4) and non-grafted-CS NPs (**F2′**, G_5) had similar EC_{50} values of (5 mg kg^{-1}) resulting in the death of 50% of the animal test population. Intriguingly, the attained EC_{50} of the TPP^+-g-CS NPs (**F2**, G_6) was significantly lower than the ungrafted NPs ($P < 0.001$) equivalent to (2.5 mg kg^{-1}). The last observation is reminiscent of the *in vitro* cytotoxicity study affirming the

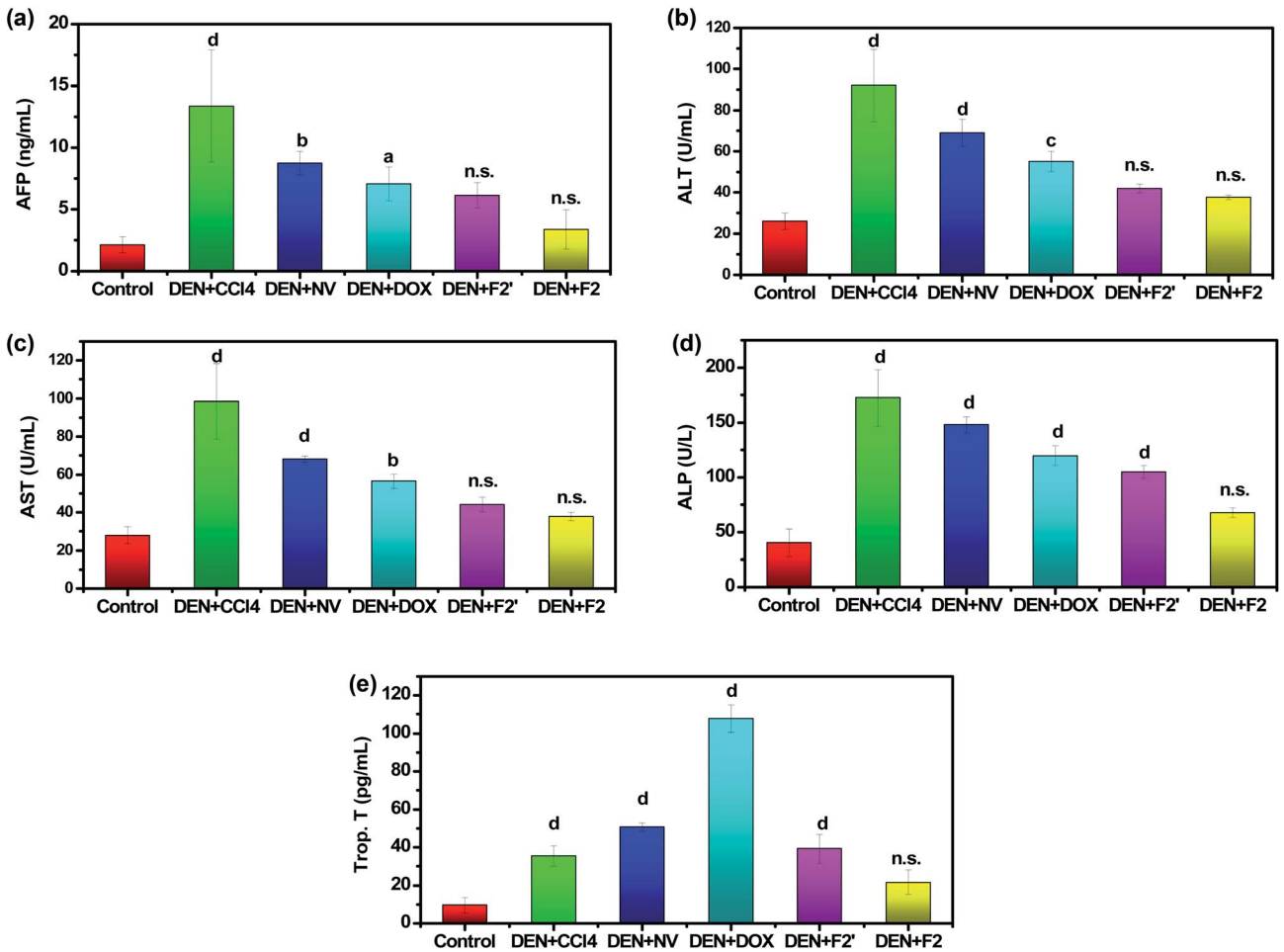

Fig. 10 Assessment of the antitumor effect and biological toxicity of DOX-SAL/CS core–shell NPs using hepatocellular carcinoma (HCC-bearing) *in vivo* animal model (a) AFP hepatic protein level, (b) ALT hepatic enzyme activity, (c) AST hepatic enzyme activity, (d) ALP hepatic enzyme activity, and (e) troponin-T cardiac protein level. Results presented as mean ± SD ($n = 9$), statistical significance is relative to control ($^aP \leq 0.05$, $^bP \leq 0.01$, $^cP \leq 0.001$, $^dP \leq 0.0001$).

enhanced antiproliferative efficiency owing to the mitochondrial targeting.

The evaluation of alanine aminotransferase (ALT) enzyme levels in the serum was investigated to assess the extent of hepatic injury, Fig. 10b.[36] Findings showed that HCC induction procedure in mice caused extreme hepatotoxicity accompanied with significant increase in serum ALT levels relative to normal mice ($P < 0.0001$). This hepatotoxic effect was reversed upon treatment with both **F2′** and **F2** core–shell NPs. The restoration of normal liver functioning is evident through rendering ALT protein levels similar to the normal serum value. Unlike the DOX-loaded NPs, the treatment with drug free NVs were not able to reverse the HCC pertinent functional aberrations ($P < 0.0001$). This last finding proves that NVs do not have any antiproliferative activity by itself. Despite, being therapeutically active free DOX was not as efficient as the NPs in restoring the normal ALT levels ($P < 0.01$).

Likewise, to ALT, enhanced levels of aspartate aminotransferase (AST) protein in the blood is well correlated to hepatic diseases.[37] A similar pattern was observed for AST serum levels to that of ALT before and after treatment with NPs, Fig. 10c. Additionally, alanine aminotransferase (ALP) serum level, which is used as an HCC prognostic factor, was assessed.[38] The results showed that trend of change in ALP serum level was resembling that of ALT and AST, Fig. 10d. Interestingly, the grafted-CS NPs (**F2**) were significantly efficient in restoring ALP levels to normal, which is significantly better when compared to their non-grafted counterparts (**F2′**) ($P < 0.01$). Our findings relevant to the reduction of AST and ALP serum levels post-treatment by the developed NPs (**F2** and **F2′**) confirm that they are more therapeutically effective when compared to free DOX.

Beyond their antiproliferative capacity, the developed NPs biological toxicity profile was evaluated. The biological toxicity of the drug is an important aspect of our study as it is well reported that DOX induces severe cardiotoxicity.[39,40] To this end, the cardiotoxicity biomarker troponin-T serum level was measured, Fig. 10e.[41] As shown by the results, treatment by free DOX (G_4) caused an extremely significant cardiotoxicity as compared to normal control (G_1) ($P < 0.0001$). Compared to the free drug, treatment with the developed NPs (G_5, G_6) conferred a reduced biological toxicity profile significantly lowering the troponin-T levels ($P < 0.0001$). Taking the dose difference into account, treatment with the mitochondria targeted NPs (G_6) was

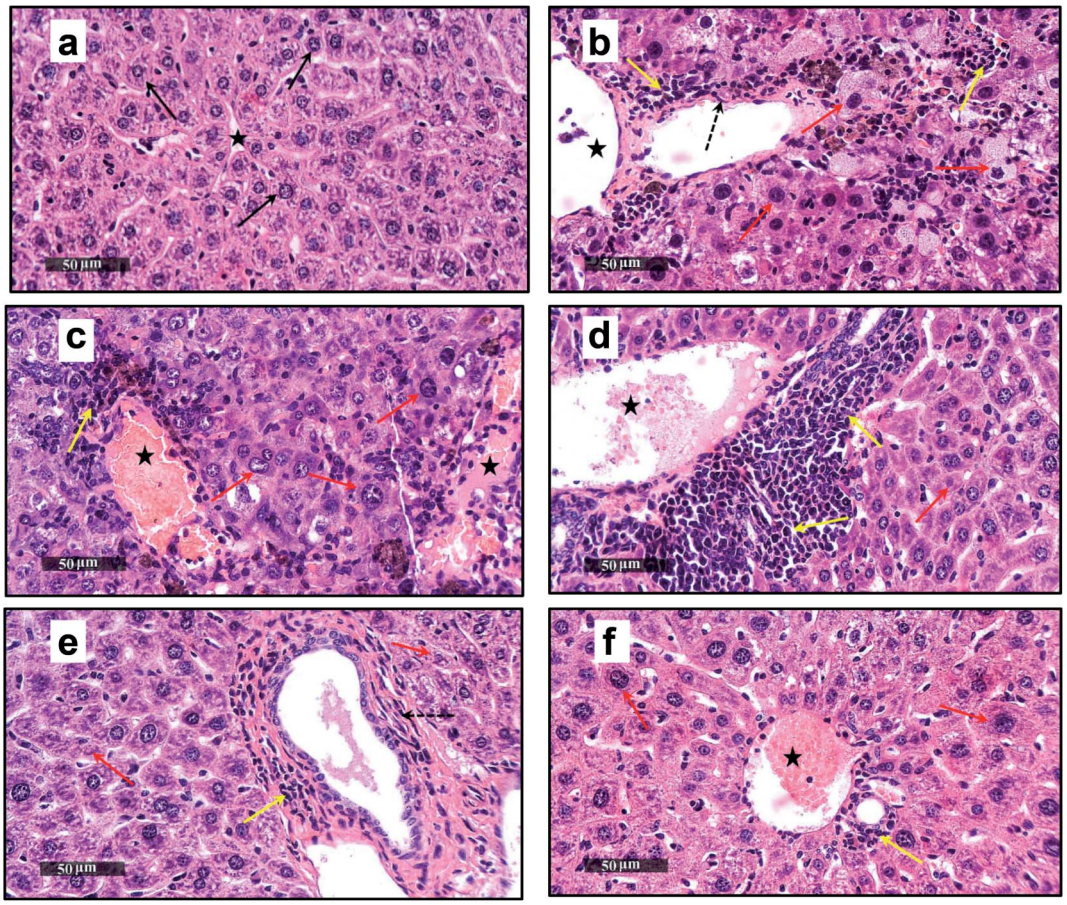

Fig. 11 Histopathological sections of the hepatic specimens extracted from (a) normal group, (b) HCC-bearing non-treated control group, (c) HCC-bearing group treated with SAL/TPP$^+$-g-CS NVs, (d) HCC-bearing group treated with pristine DOX·HCl (5 mg kg^{-1}), (e) HCC-bearing group treated with DOX-SAL/CS NPs (**F2′**) (5 mg kg^{-1}) and (f) HCC-bearing group treated with DOX-SAL/TPP$^+$-g-CS NPs (**F2**) (2.5 mg kg^{-1}). (H&E stain, scale 50 μm).

evidently safer than non-targeted NPs (G_5) ($P < 0.01$), attaining similar protein levels to the normal control.

4.7.6. Histopathological examination for liver tissues results. Microscopic examination of mice liver samples from different groups was done as shown in Fig. 11(a–e). Normal control G_1 samples demonstrated normal histological features of mouse liver in parenchyma with many obvious well-structured hepatocytes with integral subcellular details (arrow), unflawed hepatic vasculature (star) and portal areas with undamaged sinusoids were shown, Fig. 11a. Model HCC G_2 samples showed severe disorganization of histological features of hepatic parenchyma with many records of hepatomegaly with many hyperchromatic binucleated cells with prominent nucleoli (red arrow), fewer apoptotic figures were observed accompanied with moderate dilatation of hepatic blood vessels (star) severe mononuclear inflammatory cells infiltrates all over hepatic lobules and perivascular areas (yellow arrow). Significant fibroblastic activity was observed with moderate pseudo lobulation of hepatic lobules by newly formed collagen fibers dashed arrow, Fig. 11b. G_3 mice treated with CS NVs showed almost the same records as model sample with milder and nonsignificant decrease of inflammatory cell infiltrates. Fig. 11c. G_4 mice treated with free DOX.HCl showed mild dilation and congestion of hepatic BVs (star) with persistent record of perivascular inflammatory cell infiltrates (yellow arrow). Moreover, significant reduction of inflammatory cells infiltrates all over hepatic sinusoids minimal fibroblastic activity as well as minimal records of abnormal hepatocellular changes and alterations with few records of degenerated hepatocytes (red arrow), Fig. 11d. G_5 mice treated with DOX-loaded CS NPs (**F2′**) showed more organized morphological features of hepatic parenchyma with minimal scattered records of cytomegaly with hyperchromatic nuclei (red arrow), Fig. 11e. Moreover, intact vasculatures were shown (star) with minimal inflammatory cell infiltrates as well as fibroblastic activity. Finally, G_6 mice treated with DOX-loaded TPP^+-g-CS NPs (**F2**) showed almost intact hepatocellular structures with few scattered degenerated hepatocytes (red arrow). However, moderate dilation of hepatic BVS (star) with mild periportal focal inflammatory cell infiltrate (yellow arrow) and collagen fibers (dashed arrow) were shown, Fig. 11f.

Taken together, the biochemical serological testing as well as the histological examination indicated the superiority of mitochondrial targeting (G_6) in effectively inhibiting HCC progression at a significantly lower dose. Additionally, mitotropic NPs (**F2**) attained a biologically safe profile with minimized hepatotoxicity to almost null cardiotoxicity.

5. Conclusion

This study reports the development of mitotropic chitosan/sodium alginate-based core–shell nanocarriers (DOX-SAL/TPP+-g-CS NPs) for the treatment of hepatic cancer. The optimum NPs were found to exhibit favorable physicochemical characteristics mainly enhanced structural stability due to the incorporation of PVA; reflected by the enhanced drug EE% and homogenous particle size distribution. The other factor contributing to the high EE% is the electrostatic interaction between the cationic DOX with the polyanionic sodium alginate polymer. Afterwards, the mitochondria targeting was ensured through the synthesized TPP^+-g-CS polymer used as an outer coating shell. Release profiles were also evaluated and were shown to be pH dependent. Biologically, the DOX-SAL/TPP^+-g-CS NPs were found to be exclusively localized in the mitochondria, potentiating their antiproliferative activity. *In vitro* studies proved that the synthesized core–shell NPs were found to cause apoptotic cell-death and S-phase cell-cycle arrest. Finally, the *in vivo* studies proved that the designed NPs were biocompatible as reflected by the reduced cardiotoxicity and the therapeutic efficacy as presented by the retrieval of normal hepatic function and structure. Conclusively, the prepared NP system deems promising due to its enhanced therapeutic selectivity towards cancerous cells nominating it for wider application against various cancer types.

Conflicts of interest

There are no conflicts to declare.

Acknowledgements

The principal investigator and the authors would like to thank the Academy of Scientific Research and Technology (ASRT), Egypt for funding this project (JESOR-Fund).

References

1 H. Sung, *et al.*, Global Cancer Statistics 2020: GLOBOCAN Estimates of Incidence and Mortality Worldwide for 36 Cancers in 185 Countries, *Ca-Cancer J. Clin.*, 2021, **71**(3), 209–249.
2 J. K. Patra, *et al.*, Nano based drug delivery systems: recent developments and future prospects, *J. Nanobiotechnol.*, 2018, **16**(1), 71.
3 A. Z. Mirza and F. A. Siddiqui, Nanomedicine and drug delivery: a mini review, *Int. Nano Lett.*, 2014, **4**(1), 94.
4 A. V. Kabanov, *et al.*, Pluronic® block copolymers: novel functional molecules for gene therapy, *Adv. Drug Delivery Rev.*, 2002, **54**(2), 223–233.
5 R. Watkins, *et al.*, Natural product-based nanomedicine: recent advances and issues, *Int. J. Nanomed.*, 2015, **10**, 6055.
6 S. V. Boddapati, *et al.*, Mitochondriotropic liposomes, *J. Liposome Res.*, 2005, **15**(1–2), 49–58.
7 Y. Yamada and H. Harashima, Mitochondrial drug delivery systems for macromolecule and their therapeutic application to mitochondrial diseases, *Adv. Drug Delivery Rev.*, 2008, **60**(13–14), 1439–1462.
8 J. W. Nichols and Y. H. Bae, Odyssey of a cancer nanoparticle: from injection site to site of action, *Nano today*, 2012, **7**(6), 606–618.
9 L. Rajendran, H.-J. Knölker and K. Simons, Subcellular targeting strategies for drug design and delivery, *Nat. Rev. Drug Discovery*, 2010, **9**(1), 29–42.

10 M. Mossalam, A. S. Dixon and C. S. Lim, Controlling subcellular delivery to optimize therapeutic effect, *Ther. Delivery*, 2010, **1**(1), 169–193.
11 R. A. Smith, R. C. Hartley and M. P. Murphy, Mitochondria-targeted small molecule therapeutics and probes, *Antioxid. Redox Signaling*, 2011, **15**(12), 3021–3038.
12 Z.-P. Chen, *et al.*, Mitochondria-targeted drug delivery system for cancer treatment, *J. Drug Targeting*, 2016, **24**(6), 492–502.
13 Z. Wang, *et al.*, Nanopreparations for mitochondria targeting drug delivery system: current strategies and future prospective, *Asian J. Pharm. Sci.*, 2017, **12**(6), 498–508.
14 P. G. Finichiu, *et al.*, Mitochondrial accumulation of a lipophilic cation conjugated to an ionisable group depends on membrane potential, pH gradient and pK a: implications for the design of mitochondrial probes and therapies, *J. Bioenerg. Biomembr.*, 2013, **45**(1–2), 165–173.
15 S. Marrache and S. Dhar, Engineering of blended nanoparticle platform for delivery of mitochondria-acting therapeutics, *Proc. Natl. Acad. Sci.*, 2012, **109**(40), 16288–16293.
16 D. Y. Cho, *et al.*, Triphenylphosphonium-conjugated poly (ε-caprolactone)-based self-assembled nanostructures as nanosized drugs and drug delivery carriers for mitochondria-targeting synergistic anticancer drug delivery, *Adv. Funct. Mater.*, 2015, **25**(34), 5479–5491.
17 V. Kumar and S. V. Malhotra, Study on the potential anti-cancer activity of phosphonium and ammonium-based ionic liquids, *Bioorg. Med. Chem. Lett.*, 2009, **19**(16), 4643–4646.
18 B. Bachowska, *et al.*, High Cytotoxic Activity of Phosphonium Salts and Their Complementary Selectivity towards HeLa and K562 Cancer Cells: Identification of Tri-n-butyl-n-hexadecylphosphonium bromide as a Highly Potent Anti-HeLa Phosphonium Salt, *ChemistryOpen*, 2012, **1**(1), 33–38.
19 J. Shi, *et al.*, Cancer nanomedicine: progress, challenges and opportunities, *Nat. Rev. Cancer*, 2017, **17**(1), 20.
20 S. Gorini, *et al.*, Chemotherapeutic Drugs and Mitochondrial Dysfunction: Focus on Doxorubicin, Trastuzumab, and Sunitinib, *Oxid. Med. Cell. Longevity*, 2018, 7582730.
21 H. Huang, *et al.*, Antitumor activity and antitumor mechanism of triphenylphosphonium chitosan against liver carcinoma, *J. Mater. Res.*, 2018, **33**(17), 2586–2597.
22 N. P. Katuwavila, *et al.*, Chitosan-alginate nanoparticle system efficiently delivers doxorubicin to MCF-7 cells, *J. Nanomater.*, 2016, 736–747.
23 A. Hefnawy, I. A. Khalil and I. M. El-Sherbiny, Facile development of nanocomplex-in-nanoparticles for enhanced loading and selective delivery of doxorubicin to brain, *Nanomedicine*, 2017, **12**(24), 2737–2761.
24 H. K. Shaikh, R. Kshirsagar and S. Patil, Mathematical models for drug release characterization: a review, *World J. Pharm. Pharm. Sci.*, 2015, **4**, 324–338.
25 L. Wang, *et al.*, Novel water soluble phosphonium chitosan derivatives: synthesis, characterization and cytotoxicity studies, *Int. J. Biol. Macromol.*, 2011, **48**(2), 375–380.
26 T. A. Theodossiou, *et al.*, Mitochondrial delivery of doxorubicin by triphenylphosphonium-functionalized hyperbranched nanocarriers results in rapid and severe cytotoxicity, *Pharm. Res.*, 2013, **30**(11), 2832–2842.
27 J. Hou, *et al.*, Triphenyl phosphine-functionalized chitosan nanoparticles enhanced antitumor efficiency through targeted delivery of doxorubicin to mitochondria, *Nanoscale Res. Lett.*, 2017, **12**(1), 1–9.
28 H. Shagholani, S. M. Ghoreishi and M. Mousazadeh, Improvement of interaction between PVA and chitosan *via* magnetite nanoparticles for drug delivery application, *Int. J. Biol. Macromol.*, 2015, **78**, 130–136.
29 A. Kim, *et al.*, Validation of Size Estimation of Nanoparticle Tracking Analysis on Polydisperse Macromolecule Assembly, *Sci. Rep.*, 2019, **9**(1), 2639.
30 M. P. Paarakh, *et al.*, Release kinetics–concepts and applications, *Int. J. Pharm. Res. Technol.*, 2018, **8**(1), 12–20.
31 M. C. Drinane and V. H. Shah, Alcoholic hepatitis: diagnosis and prognosis, *Clinical Liver Disease*, 2013, **2**(2), 80.
32 R. Tolba, *et al.*, Diethylnitrosamine (DEN)-induced carcinogenic liver injury in mice, *Lab. Anim.*, 2015, **49**(1 Suppl), 59–69.
33 L. W. Weber, M. Boll and A. Stampfl, Hepatotoxicity and mechanism of action of haloalkanes: carbon tetrachloride as a toxicological model, *Crit. Rev. Toxicol.*, 2003, **33**(2), 105–136.
34 T. Sakurai, S. Maeda and M. K. Lufen Chang, INAUGURAL ARTICLE by a Recently Elected Academy Member: Loss of hepatic NF-κB activity enhances chemical hepatocarcinogenesis through sustained c-Jun N-terminal kinase 1 activation, *Proc. Natl. Acad. Sci. U. S. A.*, 2006, **103**(28), 10544.
35 F. Farinati, *et al.*, Diagnostic and prognostic role of α-fetoprotein in hepatocellular carcinoma: both or neither?, *Am. J. Gastroenterol.*, 2006, **101**(3), 524–532.
36 W. R. Kim, *et al.*, Serum activity of alanine aminotransferase (ALT) as an indicator of health and disease, *Hepatology*, 2008, **47**(4), 1363–1370.
37 A. Memon, *et al.*, A Modified Protocol of Diethylnitrosamine Administration in Mice to Model Hepatocellular Carcinoma, *Int. J. Mol. Sci.*, 2020, **21**(15), 5461.
38 S. Sarkar, *et al.*, Pharmaceutical efficacy of harmalol in inhibiting hepatocellular carcinoma, *J. Pharm. Sci.*, 2020, **6**(1), 1–18.
39 Y.-W. Zhang, *et al.*, Cardiomyocyte death in doxorubicin-induced cardiotoxicity, *Arch. Immunol. Ther. Exp.*, 2009, **57**(6), 435–445.
40 B. Kalyanaraman, Teaching the basics of the mechanism of doxorubicin-induced cardiotoxicity: Have we been barking up the wrong tree?, *Redox Biol.*, 2020, **29**, 101394.
41 E. H. Herman, *et al.*, Use of cardiac troponin T levels as an indicator of doxorubicin-induced cardiotoxicity, *Cancer Res.*, 1998, **58**(2), 195–197.